Effects of thermo-mechanical process on phase transitions, hydrogen solubility and corrosion of Ta-modified Zr-1Nb alloys

Ferreirós, P.A.; Savoy Polack, E.C.; Lanzani, L.A.; Alonso, P.R.; Quirós, D.P.; Mieza, J.I.; Rubiolo, G.H.

DOI:
10.1016/j.jnucmat.2021.153039

Effects of thermo-mechanical process on phase transitions, hydrogen solubility and corrosion of Ta-modified Zr-1Nb alloys

P.A. Ferreirós[a,b,c], E.C. Savoy Polack[a], L.A. Lanzani[a], P.R. Alonso[a], P.D. Quirós[a], J.I. Mieza[a], G.H. Rubiolo[a,b,*]

[a] Gerencia Materiales (GAEN) - Comisión Nacional de Energía Atómica (CNEA), Instituto Sabato - Universidad Nacional de San Martín (UNSAM), Av. Gral. Paz 1499, San Martín, Buenos Aires B1650KNA, Argentina.
[b] Consejo Nacional de Investigaciones Científicas y Técnicas (CONICET), Godoy Cruz 2290, C1425FQB Ciudad Autónoma de Buenos Aires, Argentina
[c] School of Metallurgy and Materials, University of Birmingham, Birmingham, B15 2TT, UK.

Keywords: Zr–Nb alloy, Ta addition, phase transformation, corrosion, hydrogen solubility

Abstract

The feasibility of using Ta as a minor alloying element in Zr-1Nb alloys is addressed in terms of phase stability and resistance to corrosion of the microstructure obtained with the following two thermomechanical processes after a water quenching from β_{Zr}: a) annealed at 570 °C for 3840 h and b) a combination of intermediate annealing temperatures and cold rolled steps. Hydrogen solubility was also measured, but only alloys with the first process. It was found, through calorimetric measurements, that an increase of Ta replacing Nb in the nominal alloy composition increases the $\alpha \rightarrow (\alpha + \beta)$ phase transformation temperature in agreement with an estimated increase in the enthalpy of formation of the $\beta_{Nb/Ta}$ phase, $\Delta H^{f}_{\beta_{Nb/Ta}}$. As expected, the mass fraction of $\beta_{Nb/Ta}$ measured in the rolled alloys is lower. Further, this diminution is larger in the alloys containing Ta due to the lower mobility of Ta and higher $\Delta H^{f}_{\beta_{Nb/Ta}}$. The growth of the oxide layer in each alloy, at 400 °C steam up to 14 days, follows the predictor calculated as the ratio between the atomic concentrations of Nb plus Ta in the alloy and $\Delta H^{f}_{\beta_{Nb/Ta}}$. A slight decrease in hydrogen solubility was observed at low Ta content in the alloy.

1. Introduction

The Zr-1Nb alloy is being used as an advanced cladding material for French pressurized water reactors (PWR), under the designation M5, and for similar application in Russian reactors under the designation E110. The absence of Sn in their chemical composition significantly improve corrosion and hydrogen-pickup resistance in high burnup [1]. Not only does the alloying-element content play a major role in their corrosion kinetics, but so too does its

* Corresponding author. Present address: Gerencia de Materiales, Departamento de Transformaciones y Propiedades, Comisión Nacional de Energía Atómica, Av. Gral Paz 1499, B1650KNA San Martín, Argentina.
Tel.: 054 11 6772 7240; fax: 054 11 6772 7362.
E-mail address: rubiolo@cnea.gov.ar (G.H.Rubiolo).

spatial distribution in the material. Their corrosion resistance is known to increase when equilibrium particles of β_{Nb} phase (very rich in Nb) are present instead of the metastable β_{Zr} phase (19 wt% Nb) [[2],[3],[4]]. A recent investigation provided new experimental information seeking to elucidate the oxidation behavior of Nb present in β_{Zr}, β_{Nb} and solid solution and how this is related to the macroscopic oxidation kinetics of Zr-Nb alloys [5]. The authors have shown that β_{Nb} precipitates are much more resistant to oxidation than β_{Zr} precipitates, suggesting that niobium-rich precipitates exhibit a protective effect on immediate oxidation of inner niobium, allows it to remain metallic well after oxidation of the surrounding zirconium matrix. Consequently, they also found a larger doping of the oxide with Nb in solid solution when the alloy contains β_{Zr} precipitates. Additionally, the corrosion kinetics of β_{Zr} containing alloy is parabolic, whereas that containing β_{Nb} exhibits subparabolic kinetics. Using their own model of the oxidation kinetics of zirconium alloys [6], which includes space charge effects within the oxide, they theorized that this additional Nb in the solid solution in the oxide is able to compensate for the space charge. Thus, they can correlate the parabolicity of the oxidation kinetics with the aliovalent ions dispersed in solution in the oxide; the lower the concentration of aliovalent ions in solution, the lower the spatial charge compensation and the subparabolic oxidation kinetics occurs.

Mo and Ta are two of the promising minor alloying elements for doping in Zr-Nb alloys. Both systems, Nb-Mo [7] and Nb-Ta [8], are complete solid solution systems, due to almost identical atomic radii and the same crystal structure with similar lattice parameters. The binary phase diagrams, Zr-Nb [9] and Zr-Ta [10], have similar phase fields and monotectoid reactions; instead, the Zr-Mo [11] phase diagram reports the formation of an intermetallic compound, Mo_2Zr, which can result in the formation of a new type of precipitates beyond the β_{Nb} phase. However, viewed from the material selection philosophy for nuclear fuel cladding, the thermal neutron absorption cross section of Mo (2.48 barns) is quite low, while that of Ta (20.6 barns) is too high [12]. Still, the neutron economics of replacing Nb with Ta in the Zr-1Nb alloy for use in the cladding material must be evaluated. A first estimate of the effect can be made by calculating the relative change in the macroscopic thermal neutron absorption cross section of the alloy [13]. Thus, we obtain that the macroscopic cross section increases almost linearly by substituting Nb for Ta and reaches a maximum of 19% for the total replacement. This means that the neutron economy will not change if the thickness of the cladding decreases following the same rate, but in that case the circumferential stress will increase in the same way. The effects of Mo on the mechanical properties of Zr-Nb alloys were investigated by Yang et al [14], they were able to estimate a 13% increase in the yield stress of Zr-1.2Nb caused by 0.1 wt% Mo in solid solution. Our previous investigation on the chemical composition of the precipitates and the matrix in equilibrium $(\alpha + \beta)$ Zr-1Nb alloys with Ta addition showed a matrix with 0.17 wt% Ta in solid solution [15]. Due to the almost identical atomic radii for Mo and Ta, solid solution hardening should only depend on atomic

concentration, therefore a yield stress increase of around 22% can be expected with Ta replacing Nb in the Zr-1Nb alloy. This means that the larger neutron absorption of the cladding material where Nb is replaced by Ta could be compensated by decreasing its thickness without detriment to its mechanical strength.

The development of Ta-modified Zr-Nb alloys as a new nuclear cladding material has been launched with our study mentioned above [15]. That research focused on the influence of a small addition of Ta on the phase equilibrium microstructure of the Zr-1Nb alloy aged at 570 °C. It was found that the microstructure of two phases ($\alpha_{Zr} + \beta_{Nb}$) remains, the Ta atoms mostly replace the Zr atoms in both phases and, if the substitution of Nb for Ta maintains the composition (Nb + Ta) close to 1 wt%, a decrease in the mass fraction of the β phase is observed. On the account of the fact that the precipitation behavior is unambiguously influenced by the doping of Ta, profound influence will, without doubt, be exerted on that precipitation during the manufacture procedure of the fuel cladding tube. If so, the corrosion behavior of Ta-modified Zr-1Nb alloys with different manufacturing processes is expected to be different beyond the replacement of Nb by Ta. Other interesting information to know are the hydrogen absorption characteristics of these alloys, since excessive hydrogen uptake during oxidation has a deleterious effect on the ductility of cladding material. The work presented herein attempts to answer in part these questions and elucidate if Ta addition to Zr-1Nb alloy is to be favorably considered in the future alloy development.

2. Materials and methods

2.1 Model Zr-1Nb alloys with Ta addition

The three alloys used in this study were processed from 25 g button melted in an electric arc furnace with a tungsten electrode and a water-cooled copper crucible in an argon atmosphere. The buttons were turned and remelted several times to promote chemical homogeneity. In the melting process, weight losses of less than 0.04 % were obtained. Sponge Zr (68 ± 16 ppm Hf, 148 ± 24 ppm Fe, 628 ± 63 ppm O, 30 ± 4 ppm N and 45 ± 1.5 ppm H), Nb and Ta elements with purity better than 99.9 wt% were used. Table 1 shows their nominal compositions, the absolute error in the chemical composition was estimated considering the total weight loss in the melt successively assigned to each element of the alloy.

The buttons were wrapped in a tantalum foil, encapsulated into a quartz tube which was evacuated and backfilled with argon, heat treated at 1100 °C for 30 minutes and followed by a water quenching (β_{Zr} quenched).

The alloy buttons were sectioned parallel to their axis of revolution, using a low-speed diamond saw, to extract a coupon approximately 3 cm long and 1.5 cm wide from the central

part of each button for further rolling process. The two remaining parts of the button were used to reach the microstructure of precipitated phases in thermodynamic equilibrium at 570 °C.

The formation of secondary precipitate phases (SPP) from the β_{Zr} quenched condition has already been studied in these alloys by isothermal annealing at 570 °C up to 3840 h and was reported in reference [15]. The vast majority of the SPP in the three alloys were identified as a bcc crystal structure (called β phase). The chemical composition and mass fraction of the phases present are included in Table 1. The rest of the alloys material that has reached the state of thermodynamic equilibrium at 570 °C provided two solid cylinders of approximately Ø 3.5 x 5.6 mm and a sheet of approximately 108 mm^2 in area and 1 mm thick for specific tests of the present research, both were extracted from them using electro-discharge machining (EDM).

Table 1. Chemical composition (wt%) of alloys and phases in thermodynamic equilibrium at 570 °C. Mass fraction (wt%) of both phases is also included [15].

Alloy	Phase	Chemical composition (wt%)			Mass fraction
		Zr	Nb	Ta	
Zr-1.05Nb		98.9485 ± 0.0004	1.052 ± 0.039	----	----
	α	99.43 ± 0.06	0.57 ± 0.03	----	99.42 ± 0.09
	β	17.17 ± 1.31	82.83 ± 1.31	----	0.58 ± 0.09
Zr-0.85Nb-0.20Ta		98.9483 ± 0.0003	0.851 ± 0.032	0.201 ± 0.032	-----
	α	99.30 ± 0.08	0.52 ± 0.03	0.17 ± 0.11	99.55 ± 0.09
	β	14.00 ± 0.84	73.86 ± 1.81	12.14 ± 2.65	0.45 ± 0.09
Zr-0.85Nb-0.40Ta		98.7510 ± 0.0004	0.850 ± 0.035	0.399 ± 0.035	-----
	α	99.21 ± 0.09	0.52 ± 0.03	0.27 ± 0.12	99.54 ± 0.10
	β	9.91 ± 0.75	71.35 ± 2.22	18.74 ± 2.98	0.46 ± 0.10

The coupons of the zirconium model alloys were processed in the laboratory to sheet following a sequence of steps that resemble the cold pilgering and annealing to final size of zirconium-base alloys tubing material [16]. The quenched coupon was 60% hot-rolled after a pre-heating at 570 °C for 30 min, annealing 3 hours at 570 °C in vacuum and 50% cold-rolled two times to a final thickness of 0.8 mm. The 50% cold rolling step was performed with 10 passes. Between the cold rolling steps, the sheet was annealed at 570 °C for 3 h in vacuum.

The final dimensions of the sheet were approximately 0.8x25x120 mm. Several test samples were removed from the rolled alloys sheet, EDM cut Ø 3.5 mm disc type sample and 10 mm side rectangular prism type cut with diamond saw. The grain microstructure after the rolling sequence was observed with the aid of an optical microscope and polarized light. The examined surfaces were the rolling direction (RD)–normal direction (ND) plane and they were metallographically prepared using SiC papers (1200# in the final step) and then etched with a 10HF–45HNO_3–45H_2O (vol.%) solution. The microscope used was an Olympus BX60M.

2.2 Phase analysis techniques

The final arrangement of the SPP in the microstructure of alloys was studied by light microscopy using brightfield-darkfield contrast and scanning electron microscopy (SEM) using secondary electron mode. The microscopes used were an Olympus BX60M and a FEI Quanta 200, respectively. The examined surfaces were metallographically prepared by polishing with abrasive paper up to grade 600 and etching with 10HF-45HNO_3-45$C_3H_8O_3$ (vol.%) by swabbing for 25 seconds. In the case of the rolled alloys, the examined surfaces were the RD–transverse direction (TD) plane.

During this study, high sensitivity differential scanning calorimetry (DSC) was used as a reliable tool to quantify the global mass fraction of the β_{Nb} phase present in the rolled alloys [17]. For this, the material of each alloy that has reached the state of thermodynamic equilibrium at 570 °C was used as a calibration standard for the dissolution enthalpy of the β_{Nb} phase. The transformation temperature and the dissolution enthalpy of the SPP in each thermomechanical condition of the alloy was determined from DSC measurements (Setaram LABSYS evo-DSC) with a heating rate of 5 °C/min, under an Ar (99.9997%) dynamic atmosphere of 25 ml/min. The instrument was calibrated using melting point of pure In, Sn, Al, Fe. Measurements were made in alumina crucibles that suit to the volume of a Ø 3.5 x 5.6 mm cylindrical sample. The DSC sample used for the alloys in the equilibrium state was the solid cylinder and for rolled alloys was a stack of several disks. The heat flow against temperature profile depicts the heat capacity at constant pressure of the testing sample, if an endothermic or exothermic reaction takes place, the profile shows peaks. The measured descriptors of such reactions are onset, endset, and the area under the peak calculated once the interpolated baseline of the profile is subtracted. The temperature onset of the reaction is calculated as the intersection between the baseline and a tangent line drawn on the front slope of the peak curve. Its enthalpy is calculated as the integrated area bounded by the interpolated baseline and the intersections with the peak curve. The absolute error of enthalpy was estimated by doing the same calculations with the upper and lower envelopes of the signal noise at the peak curve. When the SPP and the allotropic $\alpha_{Zr} \leftrightarrow \beta_{Zr}$ phase transformations take place in the same range of temperatures, a deconvolution of the

different enthalpic peaks is applied, assuming that the allotropic phase transformation has a lognormal Gaussian form [18].

2.3. Hydrogen solubility measurements

Hydrogen solubility was measured only in the alloy materials that has reached the thermodynamic equilibrium state at 570 °C. The second Ø 3.5 x 5.6 mm cylindrical sample of each alloy was subjected to the charge of hydrogen gas in a Sievert-type equipment to increase its hydrogen concentration by 200 wt ppm. Given the low mass of the sample, a high hydrogen concentration was chosen to obtain a higher mass fraction of hydrides and thus improve the DSC signal. Prior to the charging procedure, the surface of the sample was ground with 600-grit SiC abrasive paper. The incorporation of hydrogen in each sample was carried out at 550 °C under a hydrogen atmosphere (purity 99.999%) at low pressure (around 10 Torr). Due to the high temperature used for charging, hydrogen fully diffuse in the characteristic lengths of the sample assuring its homogeneous distribution. As far as the previous aging process is by far longer than hydriding process, it is not expected any effect on the sample microstructure.

When the hydrogen concentration in the bulk of the alloy exceeds the terminal solid solubility (TSS), hydride precipitation occurs. It is well-known that in zirconium and its alloys the TSS does not have a unique value, but depends on the direction of approach to temperature, i.e., on whether hydrides are dissolving (TSSD) or precipitating (TSSP) [19]. Among other methods, DSC allows the experimental determination of the dissolution and precipitation temperature of zirconium hydrides. A typical DSC test consist in at least three consecutive thermal cycle runs [20]. The thermal cycle is a heat up ramp from room temperature up to a maximum temperature, T_{max} , followed by a cooldown ramp to room temperature, with a hold-time of 10 min at T_{max}. The first run serves to condition the sample to a similar state before any further runs, if the responses of the next two runs are similar, i.e. the measured hydride dissolution temperatures are within 1 K, the results are considered acceptable.

The hydride transformation temperatures were measured with the same calorimeter mentioned in section 2.2. Furthermore, the crucible, the reference sample, and the atmospheric conditions were the same. The heating and cooling rates were $10\ ℃/min$ and $T_{max} = 500\ ℃$. The signals obtained from the dissolution and precipitation phenomena were processed to determine the peak temperature (PT) and the maximum slope temperature (MST), which are the most used in the literature to correlate with the TSS.

2.4. Corrosion test

Corrosion test was performed in a 4 liter static autoclave (filled with deionized water, $\kappa = 1\ \mu S/cm$) in steam at a temperature of (400 ± 10)°C and a pressure of (10 ± 1)MPa according to the ASTM G2/G2M-06 standard test [21]. This is an accelerated test used for qualifying zirconium-based alloys for use in nuclear reactor applications. It specifies use of water with a deaeration practice to reduce dissolved oxygen to low levels. To validate the 14 days corrosion tests, three Zircaloy-4 Atucha I tube coupons (named T, M and B) with known performance were used as controls. A rack and several hooks made of Zircaloy-4 allow all the test samples to be hung inside the autoclave, the control coupons were placed at the top (T), middle (M) and bottom (B) of the enclosure while the alloy Zr-Nb-Ta samples were placed in the middle part. Prior to autoclaving test, all the specimens were polished with SiC paper down to 1200 mesh and pickled with a solution of 50 vol.% deionized water + 47 vol.% HNO_3 + 3 vol.% HF. After this, they were rinsed in deionized water at 80 °C to eliminate traces of the fluoride ion coming from the pickling bath, dried with acetone and hot air and stored in a desiccator. The corrosion resistance of the specimens was evaluated by measuring their weight gain per unit area (Δw) for different durations ranging from 3 to 14 days. Before and after the test, all the specimens were weighed in an analytical balance with an accuracy of ± 0.01 mg. The Zircaloy-4 Atucha I tube coupons were measured with a caliper (accuracy ± 0.005 mm). Due to the irregular shape of the Zr-Nb-Ta alloy samples, their areas were measured from an image of the object taken with a scanner, saved as a 1200-dpi jpg image file, using AutoCAD® software. Furthermore, the length of at least one element of the object is identified and measured with the caliper. The image is inserted into AutoCAD® and scaled to the correct size using the reference lengths. Then, specific points are selected on the perimeter of the object image until all the points that enclose the area have been selected and a polyline is drawn through them. Finally, the software's Area tool calculates the area of the space enclosed by the sequence of specified points. This procedure is performed 30 times to obtain the mean and standard deviation values.

3. Results and discussion

3.1. Dependence of the SPP arrangement on thermomechanical processing

The grains morphology of the alloys after the rolling process, characterized with polarized light microscopy, is shown in Fig. 1. The results denote that a homogeneous microstructure, such as that of recrystallized grains, was formed by the additional cold rolling and annealing after a hot rolling of the β-quenched specimen. A banded structure along RD was not observed. Also, it is worth noting that is not evident a change in grain size by Ta addition. The average grain size was 4.1, 4.8 and 4.4 μm in Zr-1.05Nb, Zr-0.85Nb-0.20Ta and Zr-0.85Nb-0.40Ta specimens, respectively, which are consistent with similar values reported in reference [22] and for commercial M5® alloy [23].

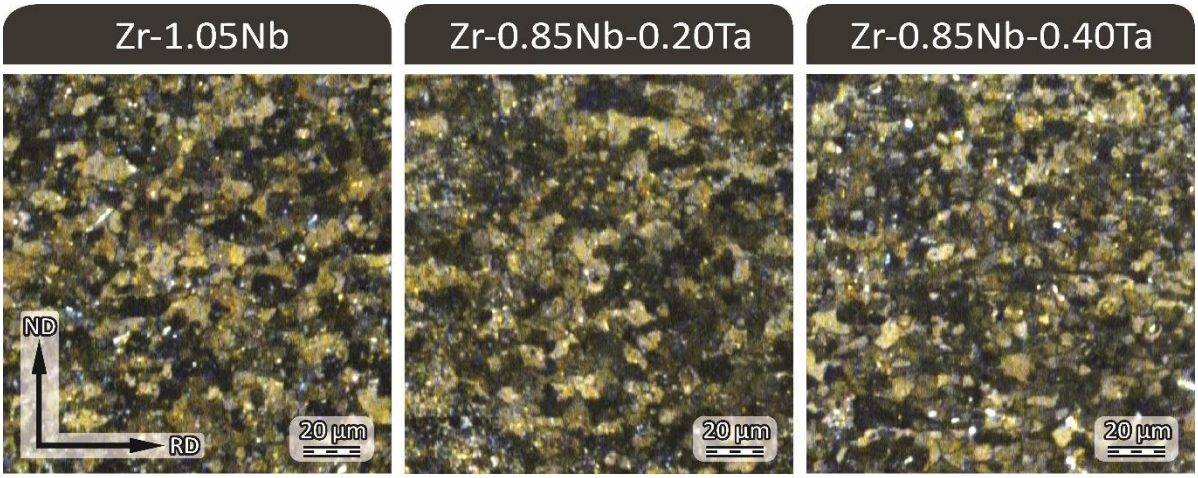

Fig. 1. Polarized optical micrographs of Ta-modified Zr-1Nb alloys after the rolling process.

The SPP´s arrangement in the alloys, after the thermal treatments of β quenching and subsequent equilibrium annealing, are showed in the optical and SEM micrographs of Figs. 2a-c and 3a-c, respectively. As discussed in reference [15], in all three alloys, the SPP´s arrangement agrees with the well-known precipitation mechanism of Zr-Nb alloys water-quenched from 1000 °C, or more, and annealed for a long time between 500 and 600 °C [[24],[25],[26]]. Precipitation occurs initially with a β phase nucleated as filaments at the needle boundaries and twin interfaces produced during the martensitic transformation $\beta \rightarrow \alpha'$, the β nuclei having the same composition as their parent α' martensitic phase. On extended ageing, a subsequent Nb enrichment of these nuclei occurs until the filaments reach the monotectoid composition β_m, a further Nb enrichment starts the decomposition of the filaments with two-components, one is a Nb-rich precipitate and the other corresponds to the α_{Zr} phase. The preferential precipitation at the needle boundaries can be seen from the bright field–dark field combination in the optical image of the same zone. The formation of a finer arrangement of smaller precipitates within the needles and along straight narrow bands marking the twin-boundary precipitation is shown in the SEM images. The platelike morphology of the SPP´s, instead of the spherical one, represents the equilibrium form of non-coherent particles of β_{Nb} phase (its chemical composition and mass fraction is given in Table 1 for each alloy).

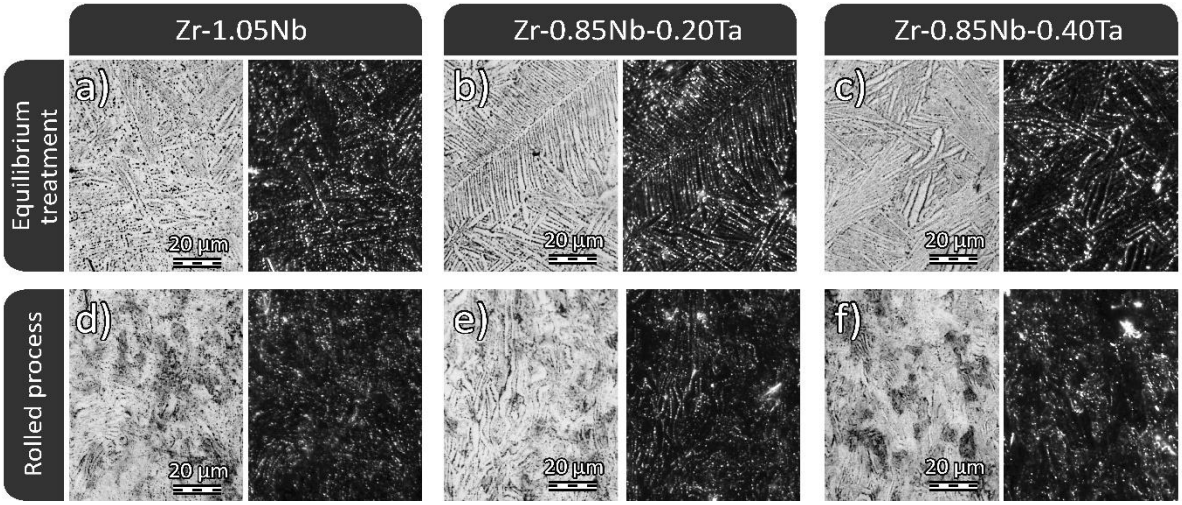

Fig. 2. Optical micrographs of alloys with equilibrium treatment and rolling process. At right are the dark fields in which the precipitates are highlighted.

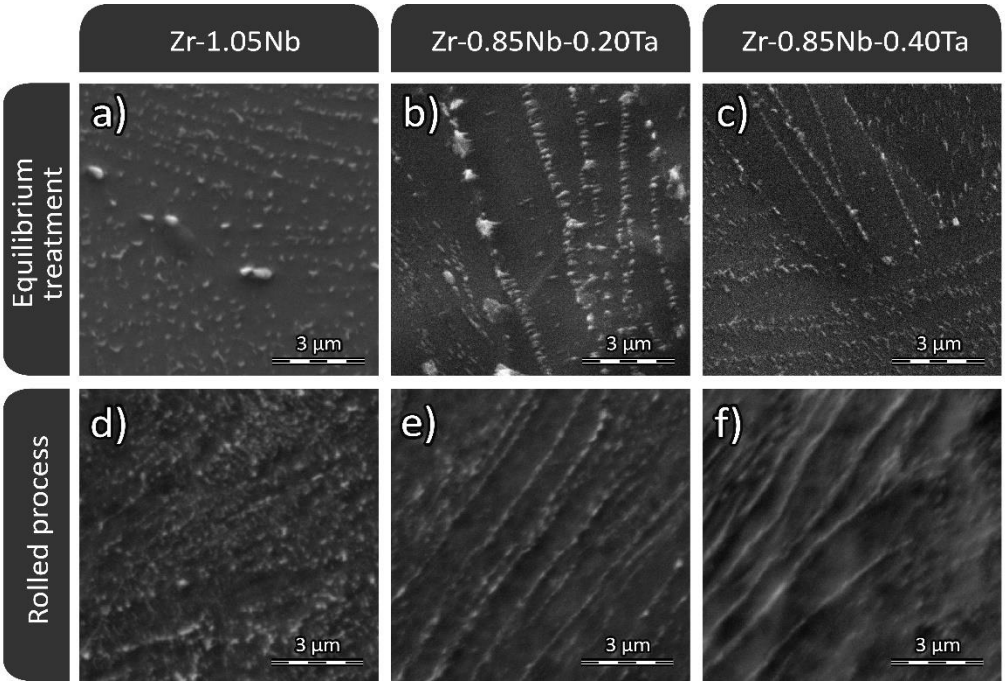

Fig. 3. SEM micrographs of alloys with the equilibrium treatment and the rolling process.

Figs. 2(d), (e) and (f) show the optical microstructures after the rolling process of the alloys in relation to its Ta content. The SPP´s are arranged along wandering narrow bands that go through several recrystallized grains. When looking at this arrangement in more detail, as in the SEM micrographs in Figs. 3(d), (e) and (f), it is seen that a band line may have separate

small precipitates if the alloy does not contain Ta or large elongated precipitates if it does. These results allow us to assume that filaments of β phase arranged in narrow bands are formed in the β-quenched martensite structure during preheating for 30 min at 570 °C. Subsequent hot and cold rolling processes make these bands wavy and wandering. Cold deformation adds the elastic energy necessary for the recrystallization process during intermediate annealing, the decomposition of β phase filaments also start during those annealing. The following section shows the results of the DSC measurements used to estimate the mass fraction of β_{Nb} phase precipitated during that β phase decomposition.

3.2. Beta niobium to beta zirconium transformation studies.

At the end of thermal treatments of β quenching and subsequent equilibrium annealing, each alloy is studied by calorimetry. Each test consists of a heating/cooling cycle in the range 450-1000 °C.

Fig. 4(a) represents a portion of the calorimetry thermogram obtained on heating. To enhance clarity, we have sketched only the transformation profile zone using the base-line subtracted DSC profiles. Two endothermic peaks are present: the first one corresponds to the dissolution of the β_{Nb} (into β_{Zr}), and the second one corresponds to the overall allotropic transformation $\alpha_{Zr} \rightarrow \beta_{Zr}$. On cooling, not shown here, the rate of temperature change prevents the formation of the β_{Nb} precipitate and, therefore, only the peak corresponding to the allotropic transformation $\beta_{Zr} \rightarrow \alpha_{Zr}$ is observed. Although the ending temperature for the allotropic transformation during cooling is imprecise, it is close to the starting temperature of the dissolution of the β_{Nb} precipitate. Therefore, this evidence implies a monotectoid transformation. The monotectoid temperature of the alloy is indicated by an arrow in each thermogram of the Fig. 4(a) and reflects an increase as the content of Ta increases.

The enthalpy change associate with the dissolution of the β_{Nb} precipitates can be estimated from the area under the peak observed in the plot of the heat flux per gram, $(\dot{Q}/m_s)$, of the alloy sample along the range temperature where this reaction occurs. To first order, this enthalpy change is proportional to the SPP´s mass fraction $C_{\beta_{Nb}}$ in such a way that [27]

$$\int \frac{\dot{Q}}{m_s}\, dT = v_T \times \frac{\Delta H}{m_s} = v_T \times \frac{\Delta H_{\beta_{Nb}\rightarrow\beta_{Zr}}\, m_{\beta_{Nb}}}{m_s} = v_T \times\ C_{\beta_{Nb}} \times \frac{\Delta H^{molar}_{\beta_{Nb}\rightarrow\beta_{Zr}}}{M_w} \qquad (1)$$

where $\Delta H_{\beta_{Nb}\rightarrow\beta_{Zr}}$ and $\Delta H^{molar}_{\beta_{Nb}\rightarrow\beta_{Zr}}$ are the mass and molar enthalpy change for the cited reaction, respectively; M_w is the molecular weight of the β_{Nb} precipitate and v_T is the heat rate. Table 2 shows the experimental values obtained for both definitions of the dissolution enthalpy, mass fraction and chemical composition of beta precipitates are those from Table 1, the estimate errors come from propagation in eq. (1) including the error of the area under the peak. The deconvolution of the different enthalpic peaks is also shown in the Fig 4(a). A

third net reaction appears at the end of the allotropic transformation in the case of the alloy containing 0.2Ta, this phase transformation was not identified.

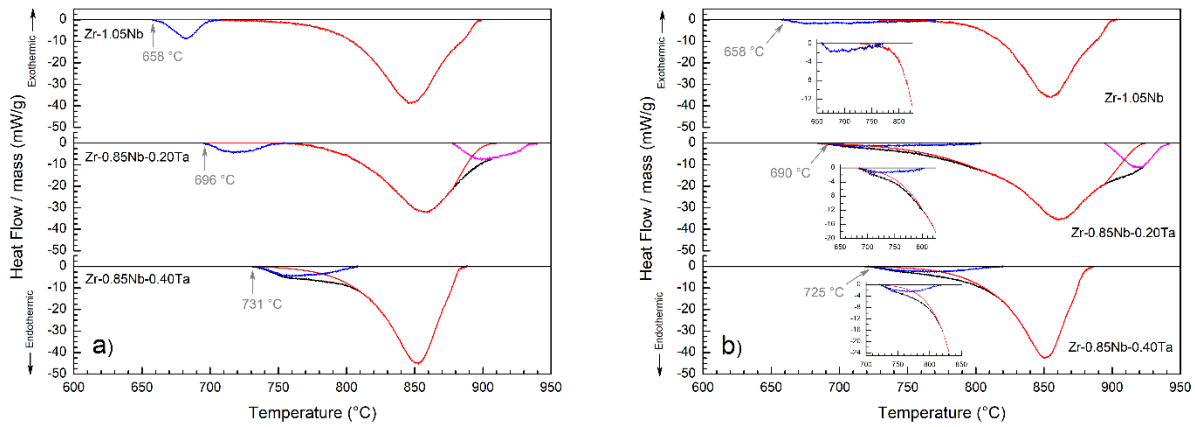

Fig. 4. Baseline-corrected DSC curves obtained on heating of the alloys after a) equilibrium annealing and b) rolling process. SPP´s dissolution peak (blue line); allotropic transformation (red line), unidentified third phase transformation (magenta line).

Table 2. The $\beta_{Nb/Ta} \rightarrow \beta_{Zr}$ transformation enthalpy obtained with calorimetric thermograms of alloy samples in thermodynamic equilibrium at 570 °C.

Alloy	$\Delta H/m_s$	$\Delta H_{\beta_{Nb}\rightarrow\beta_{Zr}}$	M_w	$\Delta H^{molar}_{\beta_{Nb}\rightarrow\beta_{Zr}}$	$\Delta H^{f}_{\beta_{Nb/Ta}}$
	(J/g)	(J/g)	(g)	(kJ/mol)	(kJ/mol)
Zr-1.05Nb	2.05 ± 0.01	354 ± 57	92.61	33 ± 5	30.0 ± 0.2
Zr-0.85Nb-0.20Ta	1.66 ± 0.12	368 ± 100	103.35	38 ± 10	32.6 ± 1.0
Zr-0.85Nb-0.40Ta	2.42 ± 0.14	526 ± 145	109.2345	57 ± 16	34.1 ± 1.2

The pioneering work of Toffolon et al. [28] reports a two times higher estimate for $\Delta H_{\beta_{Nb}\rightarrow\beta_{Zr}}$ in the Zr-1Nb alloy, in part the difference may be due to the fact that the $C_{\beta_{Nb}}$ is estimated from the nominal alloy composition and the Zr-Nb phase diagram. However, this discrepancy is not enough to justify the value obtained in the present work, particularly if we try to justify the effect of Ta on the enthalpy of dissolution of the β_{Nb} precipitates. According to the literature [29],[30], the enthalpy of formation of a precipitate of composition $M_m A_a B_b$ (where M is the majority component) from a solid solution formed by elements M, A and B , can be estimated as follows,

$$(C_A^e)^a\,(C_B^e)^b = exp\left(-\frac{\Delta H_{M_m A_a B_b}}{R\,T}\right) \qquad (2)$$

where C_A^e and C_B^e are the concentrations of the A and B elements at their solubility limit in solvent M at temperature T. Using the data from Table 1 and eq. (2) we have estimated the enthalpy of formation of the $\beta_{Nb/Ta}$ phase in our alloy samples, the results are shown in Table 2 as $\Delta H^f_{\beta_{Nb/Ta}}$. The uncertainty of the estimates was calculated by propagating errors in the eq. (2) and considering the various phase chemical compositions of Table 1. As can be seen, both our measurements and the semi-empirical thermodynamic estimates predict an increase in $\Delta H^f_{\beta_{Nb/Ta}}$ with the addition of Ta. This also agrees with the strong increase in the critical solution point of β phase observed in the binary systems Zr-Nb [31] and Zr-Ta [32]. It also appears that the values of our measurements are closer than those of Toffolon et al. to the thermodynamic predictions.

From the above results, calorimetry appears to be a powerful tool to follow the progress of phase transformations in the SPP´s during the rolling process, even for low volume fractions of them. Fig. 4(b) shows the calorimetry thermogram obtained on heating the rolled alloys. The graph inserts allow to see that the temperature range where the dissolution of the second phase particles is estimated to occur is larger than in the case of alloys in thermodynamic equilibrium at 570 °C. This can be explained by following the findings and conclusions of Toffolon et al. in reference [33], if some amount of β_{Zr} phase is present in the set of SPP´s then the allotropic transformation start temperature is over evaluated and then the peaks deconvolution returns a transformation peak of β_{Nb} phase which temperature range is larger than the real one. Therefore, the mass fraction of β_{Nb} particles estimated with the calorimetric method will be overvalued. Using eq. (1), the mass fraction of β_{Nb} particles in the rolled alloys, $C^{rolled}_{\beta_{Nb}}$, was calculated as,

$$C^{rolled}_{\beta_{Nb}} = \left\{ \left[\frac{\Delta H}{m_s} \right|^{rolled} \Big] \Big/ \left[\frac{\Delta H}{m_s} \right|^{eq} \Big] \right\} C^{eq}_{\beta_{Nb}} \tag{3}$$

where the supra-index "eq" indicates the values of the variables for the alloys in thermodynamic equilibrium. Table 3 shows the measured values of $\left[\frac{\Delta H}{m_s} \right|^{rolled} \Big]$ and those calculated for $C^{rolled}_{\beta_{Nb}}$ using the data from Table 2, the uncertainties in the latter were calculated by propagating errors in eq. (3). As expected, due to the lower mobility of Ta and higher enthalpy of formation of the $\beta_{Nb/Ta}$ phase (taken as the quantities $\Delta H^{molar}_{\beta_{Nb}\rightarrow\beta_{Zr}}$ in Table 2), the mass fraction $C^{rolled}_{\beta_{Nb}}$ is lower in alloys containing Ta.

Table 3. Mass fraction of $\beta_{Nb/Ta}$ phase from calorimetric thermograms of rolled alloys.

Alloy	$\left[\frac{\Delta H}{m_s}\right]^{rolled}$ (J/g)	$C_{\beta_{Nb}}^{rolled}$
Zr-1.05Nb	1.34 ± 0.17	0.38 ± 0.11
Zr-0.85Nb-0.20Ta	1.22 ± 0.18	0.33 ± 0.19
Zr-0.85Nb-0.40Ta	1.73 ± 0.12	0.33 ± 0.11

3.3. Hydrogen solubility

The results of the hydrogen solubility in alloys with the equilibrium annealing are summarized in Table 4. If the final hydrogen concentration of the alloy samples is determined by adding the initial hydrogen concentration of the zirconium sponge (≈ 45 ppm) to that incorporated by gaseous charging, the TSSD(PT) value of Zr-1.08Nb alloy agrees very well with that reported by Khatamian et al. [34] for Zr-1Nb alloy aged at 500 °C for 1000 h. The general conclusion can be drawn that tantalum addition to Zr-1Nb alloy has a small influence. The trend of the effect with increasing Ta content shows a decrease in hydrogen solubility at low content, but then reverses this trend and increases it at higher Ta content. The observed hysteresis between cool-down and heat-up TSS of Zr-1.08Nb agrees with that reported by Parodi et al.[35] in Zr-2.5Nb aged for 168 h at 500 °C. There is no noticeable difference in this hysteresis with the addition of Ta, the hysteresis is associated with the mechanical properties of the α_{Zr} phase [36] and they are expected to change little due to the small amount of Ta atoms added (see Table 1).

Table 4. The DSC hydride dissolution and precipitation data of alloy samples in thermodynamic equilibrium at 570 °C.

Alloy	Added hydrogen (ppm)	TSSD (°C)		TSSP (°C) $T_{max} = 500°C$ $Hold\ time = 10\ min$		ΔT (°C)	
		PT	MST	PT	MST	PT	MST
Zr-1.05Nb	198.0±5.7	414.3±0.6	432.9±1.2	345.6±0.5	371.9±0.6	68.7±1.1	61.0±1.8
Zr-0.85Nb-0.20Ta	202.0±8.2	420.5±0.6	439.7±0.7	347.1±1.2	375.9±0.4	73.4±1.8	63.8±1.1
Zr-0.85Nb-0.40Ta	198.0±9.8	412.6±0.9	429.5±0.8	339.1±1.4	376.2±0.7	73.5±2.3	53.3±1.5

Khatamian et al.[37] has discussed the correlation between the TSSD curve for hydrogen in unalloyed Zr measured by Kearns using hydrogen partitioning in diffusion couples [38] with

that obtained through DSC measurements. Their conclusion was that, within the experimental errors, both correlate well if the peak temperature in DSC measurements is used. Table 5 shows the hydrogen concentration in unalloyed Zr, $C_H^{\alpha_{Zr}}$, calculated from the Kearns´s curve using the TSSD(PT) measurements in our equilibrium aged alloys, as expected, these are lower than the total hydrogen content of them. The reason for this is the presence of β_{Nb} phase and the partitioning of hydrogen between the β_{Nb} and the α_{Zr}. If we assume that the hydrogen concentration in the α_{Zr} phase of our alloys is similar to that of unalloyed Zr (this is a valid assumption because the concentrations of Nb and Ta of this phase are low) and since we know its mass fraction (see Table 1), then we can estimate the hydrogen concentration in the β_{Nb} phase, $C_H^{\beta_{Nb}}$, through the partition of the total hydrogen, C_H^{total} , between both phases:

$$C_H^{\beta_{Nb}} = \left(C_H^{total} - \left(1 - C_{\beta_{Nb}}\right) C_H^{\alpha_{Zr}}\right)/C_{\beta_{Nb}}$$

Given the small value of the mass fraction of the β_{Nb} phase, $C_{\beta_{Nb}}$, both $C_H^{\beta_{Nb}}$ and the partition ratio, ρ_H, have high values, as shown in Table 5. The uncertainty in $C_{\beta_{Nb}}$ spreads giving rise to strong errors for the estimations of both, $C_H^{\beta_{Nb}}$ and ρ_H, however, the change in chemical composition in the β_{Nb} phase seems to have an influence on the hydrogen partition with the α_{Zr} phase.

The thermodynamic amounts of hydrogen dissolved in Nb-rich ternary alloys, $Nb_{1-x-y}Zr_xTa_y$ in solid solution (bcc), are of interest because they provide information on the hydrogen absorption characteristics of aged Zr-1Nb alloys that contain a small amount of Ta. Following the thermodynamic model proposed by Ramaprabhu [39], the enthalpy of formation of the interstitial hydrogen in the Nb bcc lattice is linearly modified with the concentration of the substitutional atoms

$$(\Delta H_H^0)_{\beta_{Nb}} = (\Delta H_H^0)_{Nb} + \omega_{H\leftrightarrow Zr}^p\, C_{Zr}^{\beta} + \omega_{H\leftrightarrow Ta}^p\, C_{Ta}^{\beta} \tag{4}$$

where $\omega_{H\leftrightarrow Zr}$ and $\omega_{H\leftrightarrow Ta}$ are the interaction energies between hydrogen and the substitutional atoms Zr and Ta, respectively. The power "p" is the number of neighboring lattice sites around a given interstice. The entropy of formation of the interstitial in the alloy is considered like that of pure Nb, $(\Delta S_H^0)_{alloy} \cong (\Delta S_H^0)_{Nb}$. Thus, considering the configuration entropy, the equilibrium hydrogen concentration in the alloy is obtained as,

$$C_H^{\beta_{Nb}} = exp\left[-\frac{(\Delta G_H^0)_{\beta_{Nb}}}{R\,T}\right] = \exp\left[-\frac{(\Delta H_H^0)_{\beta_{Nb}} - T(\Delta S_H^0)_{\beta_{Nb}}}{R\,T}\right]$$

$$C_H^{\beta_{Nb}} = \exp\left[-\frac{(\Delta H_H^0)_{Nb} - T(\Delta S_H^0)_{Nb} + \omega_{H\leftrightarrow Zr}^p\, C_{Zr}^{\beta} + \omega_{H\leftrightarrow Ta}^p\, C_{Ta}^{\beta}}{R\,T}\right]$$

$$C_H^{\beta_{Nb}} = C_H^{Nb} \exp\left[-\frac{\omega_{H\leftrightarrow Zr}^{p}\, C_{Zr}^{\beta} + \omega_{H\leftrightarrow Ta}^{p}\, C_{Ta}^{\beta}}{R\,T}\right] \quad (5)$$

Table 5 shows the hydrogen concentration in pure Nb at the hydride dissolution temperature in our alloy samples as measured, at 760 Torr, from Veleckis et al [40]. The ratio between the hydrogen concentrations in the β_{Nb} phase and pure Nb, based on the values in Table 5, passes through a minimum for the Zr-0.85Nb-0.20Ta alloy. But the concentrations C_{Zr}^{β} and C_{Ta}^{β} decrease and increase monotonically following the same sequence in the alloys (see Table 1). Therefore, the thermodynamic model thus proposed (eq. (5)) would not account for this behavior.

Table 5. The hydrogen partition between phases of alloy samples in thermodynamic equilibrium at 570 °C.

Alloy	TSSD(TP) (°C)	$C_H^{\alpha_{Zr}}$ (ppm)	$C_H^{\beta_{Nb}}$ (ppm)	ρ_H	C_H^{Nb} [40] (ppm)
Zr-1.05Nb	414.3±0.6	212.9±1.2	(5.6±1.2) 10^3	26.2±5.7	7232
Zr-0.85Nb-0.20Ta	420.5±0.6	225.7±1.3	(4.3±1.6) 10^3	19.1±7.0	7165
Zr-0.85Nb-0.40Ta	412.6±0.9	209.4±1.8	(7.7±1.6) 10^3	36.9±8.1	7250

The thermodynamic model is assuming a dilute substitutional alloy system, where the probability of finding the Zr and Ta atoms forming a complex of first neighbors is unlikely. But the higher the concentration of substitutional atoms, the higher that probability. In general, this probability is usually modeled by the product of the concentrations, so we propose to add in eq. (5) an additional term that now includes the interaction energy of hydrogen with the complex, $\omega_{H\leftrightarrow Zr\cup Ta}$, that is,

$$C_H^{\beta_{Nb}} = C_H^{Nb} \exp\left[-\frac{\omega_{H\leftrightarrow Zr}^{p}\, C_{Zr}^{\beta} + \omega_{H\leftrightarrow Ta}^{p}\, C_{Ta}^{\beta} + \omega_{H\leftrightarrow Zr\cup Ta}^{2p}\, C_{Zr}^{\beta}\, C_{Ta}^{\beta}}{R\,T}\right] \quad (6)$$

To estimate the characteristics of the pair interactions in eq. (6) we use the data in Table 5 and obtain the following results

$$\omega_{H\leftrightarrow Zr}^{p} \cong 8.6\ kJ/mol \parallel \omega_{H\leftrightarrow Ta}^{p} \cong -56.8\ kJ/mol \parallel \omega_{H\leftrightarrow Zr\cup Ta}^{2p} \cong 507.5\ kJ/mol \quad (7)$$

whose consequence on the solubility of hydrogen in the alloy rich in Nb is better displayed in the Fig 5. The orange-colored surface of the plot indicates the chemical composition of the β_{Nb} phase where the free energy of formation of interstitial hydrogen in the alloy is greater than in pure Nb, that is, the solubility of H decreases in the alloy with respect to pure Nb. The opposite effect occurs on the green colored surface. This result is in agreement with the findings known in the literature [[41],[42]], solute atoms with a size smaller than the solvent, for example V (1.34 Å) and Mo (1.36 Å) in Nb (1.43 Å), increase the terminal solubility

of hydrogen (TSH) rapidly as the solute concentration increases, while solutes with slightly larger sizes, for example Ta (1.44 Å) in Nb, also increase TSH but less rapidly. The cases of large solute sizes, such as Zr (1.54 Å) in Nb, were not specifically studied for hydrogen. However, Szkopiak et al.[43] have studied, by the internal friction technique, the solute-interstitial (s-i) interactions in thirteen niobium-1 at% substitutional alloys containing oxygen and nitrogen as interstitial solutes. They find that the lowest s-i interaction occurs between Zr or Hf with both interstitial atoms. In the ternary bcc alloys, the effect of the pairing of substitute solute atoms on the s-i interaction was also studied with the same experimental technique [44]. Our results show that given a concentration of Zr in Nb, the addition of isolated Ta atoms should increase the solubility of hydrogen, but the pairing of a few Zr and Ta atoms retards the effect.

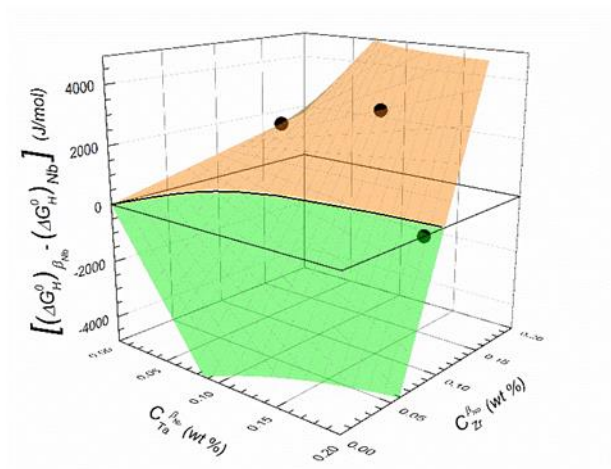

Fig. 5. Free energy difference for interstitial hydrogen formation in β_{Nb} phase and in pure Nb as a function of the concentration of Zr, C_{Zr}^{β}, and Ta, C_{Ta}^{β} . The surface is calculated with the values of interaction energies in eq. (7) while the symbols indicate the isolated values calculate with C_{Zr}^{β} and C_{Ta}^{β} given in Table 1.

3.4. Corrosion characteristics

The weight gains for Zircaloy-4 control coupons (T, M and B) under steam corrosion at 400 °C and 10 MPa for 14 days were in the range $25.0 \pm 1.8\ mg/dm^2$ and the oxide visual appearance was uniform, black, lustrous and adherent which shows that the test achieved the establish requirements for Zircaloys alloys in the standard test [21] and was valid. Furthermore, the oxide film on all the Zr-Nb-Ta alloys studied resembles that of the Zircaloy-4 control coupons, except for a dark gray color instead of black.

Fig. 6 shows the effect of thermo-mechanical processing and tantalum addition on the corrosion behavior of Zr-1Nb alloys. Regardless of the thermomechanical processes used, the weight gain of the alloys with equilibrium annealing or rolling process are within the

range $(18.3 \leq \Delta w \leq 38.1)\ mg/dm^2$ required for the Zircaloy alloys [21]. The corrosion test carried out in this investigation is mainly used as zirconium alloys' acceptance test according to ASTM G2/G2M-06 standard, but in such a role, establishes a tolerance and, therefore, has been widely used in new alloys' development. In this sense, it seems appropriate to provide an in-depth analysis of the results obtained.

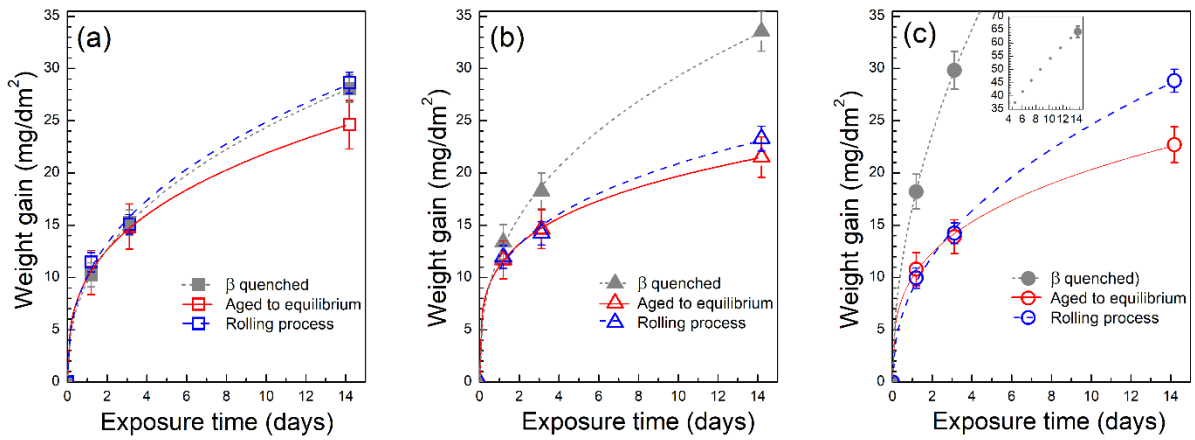

Fig. 6. The effects of thermo-mechanical processing and tantalum addition on the corrosion behavior of Zr-1Nb alloys corroded at 400 °C steam for 14 days: a) Zr-1.05Nb; b) Zr-0.85Nb-0.20Ta and c) Zr-0.85Nb-0.40Ta

The analysis starts observing that the weight gain of the water-quenched specimens is higher than those that have reached the state of thermodynamic equilibrium at 570 °C. This behavior was studied by Jeong et al. [[2],[3]] in Zr-Nb alloys. The first study [2] showed that if the Nb content in the alloy is greater than 0.6 wt%, the resistance to corrosion of the water-quenched sample decreases as the amount of Nb in the supersaturated state increases above that Nb concentration limit. However, for the alloy without Ta, the decrease in corrosion resistance in our experiment is less than in Jeong's. The difference is largely due to the amount of Nb in the supersaturated state in both water-quenched samples. Our alloy sample was extracted from a button that was water-quenched from beta phase, while Jeong's samples are pieces of water-quenched sheet metal, this makes for a much lower cooling rate for our sample. When the cooling rate is slowed down to about 100°C/s, the filaments of the β phase nucleate early at the needle boundaries and twin interfaces produced during the martensitic transformation β→α´ and part of Nb atoms segregate within them [[45],[46]]. Accordingly, the Nb in the supersaturated matrix is lower than that obtained at higher cooling rate and the corrosion resistance increases [2]. As the cooling rate was the same for buttons with and without Ta, the same loss of Nb is expected in the supersaturated matrix of samples with Ta added, but Nb diffuses faster than Ta in Zr [47], therefore, Ta should remain in the supersaturated state in the matrix. In addition, if Ta in solution is as detrimental as Nb for corrosion resistance of zirconium, the corrosion behavior

shown in Fig. 6 by the water-quenched samples containing Ta is consistent with the hypotheses stated.

If the previous analysis is applied to the samples in thermodynamic equilibrium at 570 °C, which its Nb plus Ta content in the α_{Zr} matrix is taken from Table 1, it predicts a monotonous deterioration in corrosion resistance with increasing content of Ta added to the alloy, but this is not the case, both alloys containing Ta show a tendency to increase corrosion resistance in 14 days with respect to which does not contain it and the highest resistance would be for the alloy Zr-0.85Nb-0.20Ta. In reference [3] Jeong et al. show the results of the corrosion resistance of the water-quenched Zr-Nb samples of reference [2] which were annealed for 500 hs at 570 °C to obtain the $\alpha_{Zr} + \beta_{Nb}$ phase equilibrium. At high Nb contents of 1.0-5.0 wt%, the formation of the β_{Nb} phase resulted in the reduction of the Nb concentration in the α_{Zr} matrix and the corrosion resistance was improved, but the improvement remained nearly steady with the β_{Nb} volume fraction. Therefore, our results with the addition of Ta to the β_{Nb} phase imply that its chemical composition is important for the corrosive behavior of the alloy. In the following lines we will try to understand this matter.

In the studies by Moorehead et al. [5] on the role of Nb in the oxidation kinetics of Zr-Nb alloys, they conclude that the parabolicity of this kinetics is governed, in part, by the space charge in the oxide layer. This space charge can be compensated by solute aliovalent Nb ions spread out in the oxide. The source of these ions are the various phases of the alloy, and the atomic order of those phases seems to have effect in their dissolution kinetics, for example, these researchers demonstrated that β_{Zr} precipitates dissolve faster than β_{Nb} precipitates therefore, the latter are more effective in retaining Nb and retarding the growth of the oxide layer. Since the corrosion tests for the different microstructures of the same alloy were carried out simultaneously in a single aqueous corrosive environment, the change in chemical activity of the various species due to the change in the thermodynamic equilibrium of the phases shows a magnitude able to produce a significant change in the corrosion behavior of this kind of alloy [48]. With these ideas in mind and thinking about the corrosion resistance in ours samples in thermodynamic equilibrium at 570 °C, we observe in Table 2 that the estimated enthalpy of formation of the $\beta_{Nb/Ta}$ phase, $\Delta H^{f}_{\beta_{Nb/Ta}}$, increases with the Ta added to the alloy, and since the alloy is biphasic, this means that the activity of Nb and Ta also increases in the α matrix and therefore the dissolution kinetic of both phases decrease.

In summary, one can expect the growth of the oxide layer to be proportional to the atomic concentration of Nb plus Ta and inversely proportional to the chemical activity of these species. Fig. 7a shows the atomic concentrations of Nb and Ta in the alloy and in the α phase for the three samples, and the enthalpy of formation of the $\beta_{Nb/Ta}$ phase indicative of the chemical activity of the species in the equilibrium phases. Fig. 7b shows the ratio between

the sum of atomic concentrations and the formation enthalpy, that is, a predictor of the growth behavior of the oxide layer. Comparing the predictor and the experimental observations in Fig. 6, we see that the predictor calculated with the atomic concentrations of Nb plus Ta in the alloy correctly predicts them while the one calculated only with the sum of the concentrations in the matrix does not. The decomposition of β_{Zr} precipitates during the thermomechanical rolling and annealing process causes the chemical activity of the species to gradually increase towards the maximum value at the phase equilibrium, therefore, the growth rate of the oxide layer should be expected intermediate between that observed in the quenched sample and the sample in thermodynamic equilibrium, as can be seen in all the cases illustrated in Fig. 6.

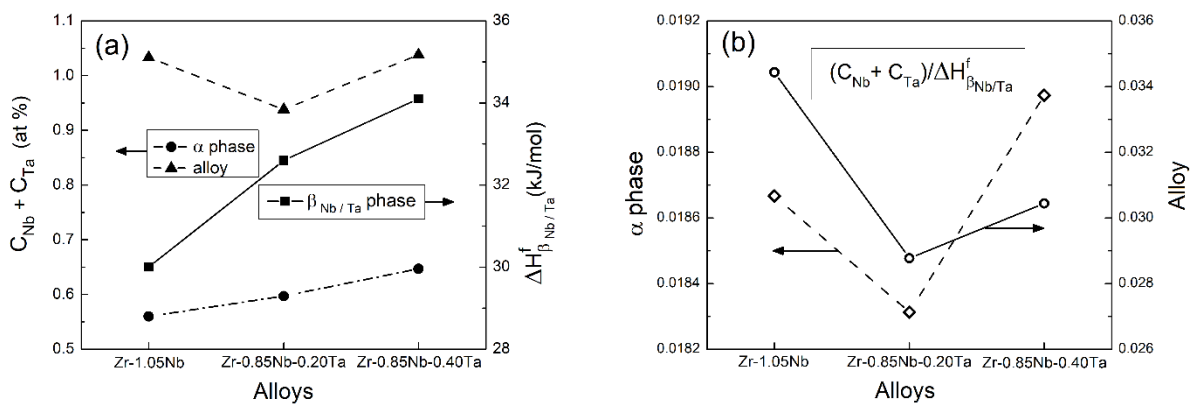

Fig. 7. Predictor of the growth behavior of the oxide layer, at 400 °C steam for 14 days, in samples of Zr-1Nb alloys added with Ta and aged until equilibrium at 570 °C.

4. Conclusions

The results of our research indicate that a small addition of Ta maintains the biphasic microstructure of Zr-1Nb nuclear alloys by increasing their monotectoid transformation temperature and their resistance to corrosion. Although a slight decrease in hydrogen solubility was observed at low Ta content.

Even though the corrosion resistance testing of the Ta-containing experimental alloys should continue to corroborate the outstanding trend observed at 14 days, it is worth further research of the Zr-1Nb-xTa alloy system as a candidate material for applications in the nuclear reactor core. Mainly when considering the higher thermal microstructural stability compared to Ta-free Zr-1Nb alloys. This could provide advantages such as a possible increase in operating temperature by tens of degrees or, similarly, seeking an acceleration in precipitation kinetics during thermomechanical processes.

Acknowledgments

This study was supported by FonCyT, through PICT-2015-2267 project, and by UNSAM, through PAI-2017-C079 project. P.A. Ferreirós acknowledges funding from the UK Engineering and Physical Sciences Research Council (EPSRC) Grant EP/T01220X/1.

References

[1] Z. Duan, H. Yang, Y. Satoh, K. Murakami, S. Kano, Z. Zhao, J. Shen, H. Abe, Current status of materials development of nuclear fuel cladding tubes for light water reactors, Nuclear Engineering and Design. (2017). https://doi.org/10.1016/j.nucengdes.2017.02.031.

[2] Y.H. Jeong, K.O. Lee, H.G. Kim, Correlation between microstructure and corrosion behavior of Zr-Nb binary alloy, Journal of Nuclear Materials. (2002). https://doi.org/10.1016/S0022-3115(02)00703-1.

[3] Y.H. Jeong, H.G. Kim, T.H. Kim, Effect of β phase, precipitate and Nb-concentration in matrix on corrosion and oxide characteristics of Zr-xNb alloys, Journal of Nuclear Materials. (2003). https://doi.org/10.1016/S0022-3115(02)01676-8.

[4] H.G. Kim, Y.H. Jeong, T.H. Kim, Effect of isothermal annealing on the corrosion behavior of Zr-xNb alloys, Journal of Nuclear Materials. (2004). https://doi.org/10.1016/j.jnucmat.2004.01.015.

[5] M. Moorehead, Z. Yu, L. Borrel, J. Hu, Z. Cai, A. Couet, Comprehensive investigation of the role of Nb on the oxidation kinetics of Zr-Nb alloys, Corrosion Science. (2019). https://doi.org/10.1016/j.corsci.2019.04.017.

[6] A. Couet, A.T. Motta, A. Ambard, The coupled current charge compensation model for zirconium alloy fuel cladding oxidation: I. Parabolic oxidation of zirconium alloys, Corrosion Science. (2015). https://doi.org/10.1016/j.corsci.2015.07.003.

[7] H. Okamoto, Mo-Nb (Molybdenum-Niobium), Journal of Phase Equilibria. (1991). https://doi.org/10.1007/BF02645086.

[8] Y. Liu, G. Wang, J. Wang, Z. Kang, Mobilities and diffusivities for bcc Nb-W, Nb-Ta, Zr-Mo and Zr-Hf alloys, Journal of Alloys and Compounds. (2013). https://doi.org/10.1016/j.jallcom.2012.11.163.

[9] H. Okamoto, Nb-Zr (niobium-zirconium), Journal of Phase Equilibria. (1992). https://doi.org/10.1007/BF02665776.

[10] H. Okamoto, Ta-Zr (tantalum-zirconium), Journal of Phase Equilibria. (1996). https://doi.org/10.1007/BF02666009.

[11] H. Okamoto, Mo-Zr (Molybdenum-Zirconium), Journal of Phase Equilibria & Diffusion. (2004). https://doi.org/10.1361/15477030420935.

[12] C.R.F. Azevedo, Selection of fuel cladding material for nuclear fission reactors, Engineering Failure Analysis. (2011). https://doi.org/10.1016/j.engfailanal.2011.06.010.

[13] DOE-HDBK-1019/1-93, DOE Fundamentals Handbook, Nuclear Physics and Reactor Theory, Vol. 1 of 2, Washington D.C., 1993.

[14] H.L. Yang, H. Abe, S. Kano, Y. Matsukawa, Y. Satoh, Effects of molybdenum on microstructural evolution and mechanical properties in Zr-Nb alloys as nuclear fuel cladding materials, in: Journal of Nuclear Science and Technology, 2015. https://doi.org/10.1080/00223131.2015.1040863.

[15] P.A. Ferreirós, P.R. Alonso, D.P. Quirós, E. Zelaya, G.H. Rubiolo, Accurate quantitative EDS-TEM analysis of precipitates and matrix in equilibrium (α+β) Zr–1Nb alloys with Ta addition, Journal of Alloys and Compounds. (2020). https://doi.org/10.1016/j.jallcom.2020.156372.

[16] D.C. J P Mardon, J Sevenat, Method of manufacturing a tube for a nuclear fuel assembly, and tubes obtained thereby. US patent US 005648995, 1997.

[17] C. Toffolon, J.C. Brachet, T. Guilbert, D. Hamon, S. Urvoy, C. Servant, D. Charquet, L. Legras, J.P. Mardon, Vieillissement thermique des alliages de zirconium-niobium en phase α (570 °c), Journal De Physique. IV : JP. (2001). https://doi.org/10.1051/jp4:2001110.

[18] T. Forgeron, J.C. Brachet, F. Barcelo, A. Castaing, J. Hivroz, J.P. Mardon, C. Bernaudat, Experiment and modeling of advanced fuel rod cladding behavior under LOCA conditions: Alpha-beta phase transformation kinetics and EDGAR methodology, in: ASTM Special Technical Publication, 2000. https://doi.org/10.1520/stp14303s.

[19] C.D.C. D. Khatamian, Z.L. Pan, M.P. Puls, Hydrogen solubility limits in Excel, an experimental zirconium-based alloy, Journal of Alloys and Compounds. 231 (1995) 488–493.

[20] IAEA – TECDOC – 1609. Intercomparison of techniques for inspection and diagnostics of Heavy Water Reactor Pressures Tubes. Determination of hydrogen concentration and Blister characterization., IAEA, Viena, Viena, Austria, 2009.

[21] Standard Test Method for Corrosion Testing of Products of Zirconium, Hafnium, and Their Alloys in Water at 680 °F or in Steam at 750 °F, in: ASTM G2/G2M-06, ASTM International, West Conshohocken, PA, 2011.

[22] H. Tian, X. Wang, W. Gong, J. Zhou, H. Zhang, Recrystallization behavior of cold-rolled Zr-1Nb alloy, Journal of Nuclear Materials. (2015).

https://doi.org/10.1016/j.jnucmat.2014.09.084.

[23] M. Rautenberg, X. Feaugas, D. Poquillon, J.M. Cloué, Microstructural characterization of creep anisotropy at 673 K in the M5® alloy, Acta Materialia. (2012). https://doi.org/10.1016/j.actamat.2012.04.001.

[24] C.D. Williams, R.W. Gilbert, Tempered structures of a Zr-2.5 wt % Nb alloy, Journal of Nuclear Materials. (1966). https://doi.org/10.1016/0022-3115(66)90078-X.

[25] S. Banerjee, S.J. Vijayakar, R. Krishnan, Precipitation in zirconium-niobium martensites, Journal of Nuclear Materials. (1976). https://doi.org/10.1016/0022-3115(76)90019-2.

[26] S. Neogy, D. Srivastava, J.K. Chakravartty, G.K. Dey, S. Banerjee, Microstructural evolution in Zr-1Nb and Zr-1Nb-1Sn-0.1Fe alloys, Metallurgical and Materials Transactions A: Physical Metallurgy and Materials Science. (2007). https://doi.org/10.1007/s11661-006-9026-0.

[27] E. Hersent, J.H. Driver, D. Piot, Modelling differential scanning calorimetry curves of precipitation in Al-Cu-Mg, Scripta Materialia. (2010). https://doi.org/10.1016/j.scriptamat.2009.12.009.

[28] J.C.B. C. Toffolon-Masclet, T. Guilbert, Study of secondary intermetallic phase precipitation/dissolution in Zr alloys by high temperature–high sensitivity calorimetry, Journal of Nuclear Materials. 372 (2008) 367–378.

[29] M. Van Rooyen, E.J. Mittemeijer, Precipitation of silicon in aluminum-silicon: a calorimetric analysis of liquid-quenched and solid-quenched alloys, Metallurgical Transactions. A, Physical Metallurgy and Materials Science. (1989). https://doi.org/10.1007/bf02647402.

[30] M.J. Starink, P.J. Gregson, A quantitative interpretation of DSC experiments on quenched and aged SiCp reinforced 8090 alloys, Scripta Metallurgica et Materiala. (1995). https://doi.org/10.1016/0956-716X(95)00317-O.

[31] P.E.J. Flewitt, A re-assessment of the monotectoid loop (β-Nb+β-Zr) in the niobium–zirconium system, Journal of Applied Crystallography. (1972). https://doi.org/10.1107/s0021889872010076.

[32] W.L. Williams, D E; Jackson, R J; Larsen, The Tantalum-Zirconium alloy system, Trans. Met. Soc. AIME. 224 (1962) 751-756.

[33] C. Toffolon, J.C. Brachet, C. Servant, L. Legras, D. Charquet, P. Barberis, J.P. Mardon, Experimental study and preliminary thermodynamic calculations of the pseudo-ternary Zr-Nb-Fe-(O,Sn) system, in: ASTM Special Technical Publication, 2002. https://doi.org/10.1520/stp11397s.

[34] D. Khatamian, Solubility and partitioning of hydrogen in metastable Zr-based alloys

used in the nuclear industry, Journal of Alloys and Compounds. (1999). https://doi.org/10.1016/S0925-8388(99)00388-6.

[35] S.A. Parodi, L.M.E. Ponzoni, M.E. De Las Heras, J.I. Mieza, G. Domizzi, Study of variables that affect hydrogen solubility in α + β Zr-alloys, Journal of Nuclear Materials. (2016). https://doi.org/10.1016/j.jnucmat.2016.05.027.

[36] Y.Y. Earmme, W.C. Johnson, J.K. Lee, PLASTIC RELAXATION OF THE TRANSFORMATION STRAIN ENERGY OF A MISFITTING SPHERICAL PRECIPITATE: LINEAR AND POWER-LAW STRAIN HARDENING., Metallurgical Transactions. A, Physical Metallurgy and Materials Science. (1981). https://doi.org/10.1007/bf02643699.

[37] D. Khatamian, V.C. Ling, Hydrogen solubility limits in α- and β-zirconium, Journal of Alloys and Compounds. (1997). https://doi.org/10.1016/S0925-8388(96)02947-7.

[38] J.J. Kearns, Terminal solubility and partitioning of hydrogen in the alpha phase of zirconium, Zircaloy-2 and Zircaloy-4, Journal of Nuclear Materials. (1967). https://doi.org/10.1016/0022-3115(67)90047-5.

[39] S. Ramaprabhu, Thermodynamics and stability of dissolved hydrogen in pd rich binary Pd1-xZx and ternary Pd1-x-yZxZy' solid solution alloys, International Journal of Hydrogen Energy. (1998). https://doi.org/10.1016/s0360-3199(97)00127-4.

[40] E. Veleckis, R.K. Edwards, Thermodynamic properties in the systems vanadium-hydrogen, niobium-hydrogen, and tantalum-hydrogen, Journal of Physical Chemistry. (1969). https://doi.org/10.1021/j100723a033.

[41] T. Matsumoto, Y. Sasaki, M. Hihara, Interaction between interstitial hydrogen and substitutional solute atoms in solid solutions of niobium-base ternary alloys, Journal of Physics and Chemistry of Solids. (1975). https://doi.org/10.1016/0022-3697(75)90013-X.

[42] D.G. Westlake, J.F. Miller, Terminal solubility of hydrogen in NbTa alloys and characterization of the solid solutions, Journal of The Less-Common Metals. (1979). https://doi.org/10.1016/0022-5088(79)90160-7.

[43] Z.C. Szkopiak, J.T. Smith, The internal friction of Nb-1 at.% substitutional alloys, Journal of Physics D: Applied Physics. (1975). https://doi.org/10.1088/0022-3727/8/11/006.

[44] M. Koiwa, Theory of the Snoek effect in ternary B.C.C. alloys V. effect of pairing of substitutional solute atoms, Philosophical Magazine. (1972). https://doi.org/10.1080/14786437208228901.

[45] A.R. Massih, T. Andersson, P. Witt, M. Dahlbäck, M. Limbäck, Effect of quenching rate on the β-to-α phase transformation structure in zirconium alloy, Journal of

Nuclear Materials. (2003). https://doi.org/10.1016/S0022-3115(03)00323-4.

[46] C. Linjiang, L. Baifeng, C. Jianwei, Z. Jun, L. Qing, Effect of cooling rate on β→α transformation during quenching of a Zr-0.85Sn-0.4Nb-0.4Fe-0.1Cr-0.05Cu alloy, Science China Technological Sciences. (2012). https://doi.org/10.1007/s11431-012-4956-9.

[47] G. Neumann, C. Tuijn, Chapter 4 Self-Diffusion and Impurity Diffusion in Group IV Metals, in: Pergamon Materials Series, 2008. https://doi.org/10.1016/S1470-1804(08)00004-7.

[48] B.G.J.S. Datta P.K., Du H.L., Corrosion of Intermetallics, in: ASM Handbook Volume 13B Corrosion: Materials, 2005: pp. 490–512.

Credit Author Statement

P.A. Ferreiros: Conceptualization, Methodology, Investigation, Formal analysis, Validation, Writing - Original Draft, Visualization

E. Savoy Polack: Investigation, Data Curation

L. Lanzani: Resources, Methodology, Formal analysis, Writing - Original Draft

P.R. Alonso: Resources, Writing - Original Draft

D.P. Quiros: Resources, Investigation.

J.I. Mieza:Resources, Investigation, Data Curation

G.H. Rubiolo: Conceptualization, Methodology, Formal analysis, Writing - review & editing, Supervision, Project administration, Funding acquisition.